Biophysical mechanisms of phase contrast in gradient echo MRI

Xiang He[a,1] and Dmitriy A. Yablonskiy[a,b,1]

Departments of [a]Radiology and [b]Physics, Washington University, One Brookings Drive, Saint Louis, MO 63130

Edited by Marcus E. Raichle, Washington University School of Medicine, St. Louis, MO, and approved June 12, 2009 (received for review May 5, 2009)

Recently reported contrast in phase images of human and animal brains obtained with gradient-recalled echo MRI holds great promise for the in vivo study of biological tissue structure with substantially improved resolution. Herein we investigate the origins of this contrast and demonstrate that it depends on the tissue "magnetic architecture" at the subcellular and cellular levels. This architecture is mostly determined by the structural arrangements of proteins, lipids, non-heme tissue iron, deoxyhemoglobin, and their magnetic susceptibilities. Such magnetic environment affects/shifts magnetic resonance (MR) frequencies of the water molecules moving/diffusing in the tissue. A theoretical framework allowing quantitative evaluation of the corresponding frequency shifts is developed based on the introduced concept of a generalized Lorentzian approximation. It takes into account both tissue architecture and its orientation with respect to the external magnetic field. Theoretical results quantitatively explain frequency contrast between GM, WM, and CSF previously reported in motor cortex area, including the absence of the contrast between WM and CSF. Comparison of theory and experiment also suggests that in a normal human brain, proteins, lipids, and non-heme iron provide comparable contributions to tissue phase contrast; however, the sign of iron and lipid contributions is opposite to the sign of contribution from proteins. These effects of cellular composition and architecture are important for quantification of tissue microstructure based on MRI phase measurements. Also theory predicts the dependence of the signal phase on the orientation of WM fibers, holding promise as additional information for fiber tracking applications.

cellular architecture | contrast mechanisms | grey matter | white matter

Conventional gradient-recalled echo (GRE) MRI phase images have been used to generate contrast in MRI of the human brain [see for example (1–3)]. This MRI contrast is profoundly enhanced at high magnetic fields (7 T and above) (4–6), allowing to visualize biological structures within gray matter (GM) and white matter (WM) that are not usually resolved with conventional MRI. Such sources as blood deoxyhemoglobin, tissue lipid, and non-heme iron content (5), as well as water-protein exchange (7) have been proposed as possible origins of the MRI signal frequency shift responsible for this contrast. Previous studies have also reported a frequency shift of 5 Hz at 3.0 T (8) and 7 Hz at 4.7 T (9) between extracellular and intracellular brain tissue ^{1}H water MRI signal, attributing this effect to magnetic susceptibility of proteins. However, none of these factors were able to fully account for the observed effects, especially the lack of the phase contrast between WM and CSF in the motor cortex area.

In this study, we demonstrate that the phase contrast of GRE MRI signal depends on the tissue architecture at the cellular and subcellular levels. The most important components of this architecture are proteins, lipids, non-heme iron, and deoxyhemoglobin that act as magnetic susceptibility inclusions, thus creating mesoscopic, tissue specific, inhomogeneous magnetic fields affecting MRI frequencies of water molecules (and/or other nuclei) moving/diffusing in their environment. We demonstrate that the observed tissue phase contrast of GRE MRI signal depends not just upon the amount of these magnetic susceptibility inclusions, but, more importantly, their spatial distribution (architecture) at the subcellular level as well as global cellular organization of brain tissue. Importantly, destruction of this architecture in diseases (e.g., multiple sclerosis) could explain changes in phase contrast reported in (10). Results are illustrated by in vivo data obtained from human brain tissue at 3 T.

Results

Theoretical Consideration—A Generalized Lorentzian Approach. It is well known that the NMR signal frequency (Larmor frequency) of the object/subject is shifted due to the magnetic susceptibility effects. It is usually assumed [see detailed discussion in (11)] that in liquid samples, this frequency shift Δf can be described as a sum of 2 terms—the first, describing effects of the object general external shape:

$$\left.\frac{\Delta f}{f_0}\right|_{\text{shape}} = A \cdot \chi, \qquad [1]$$

and the second, describing effects of the so called Lorentzian sphere:

$$\frac{\Delta f}{f_0} = \frac{4}{3}\pi \cdot \chi. \qquad [2]$$

Here f_0 is the base Larmor resonance frequency, χ is a volume magnetic susceptibility of the object and parameter A depends on the object's specific shape (note that we use CGS units throughout).

The concept of a Lorentzian sphere has played an important role in the evaluation of magnetic susceptibility effects on the water MR signal frequency shift Δf in biological systems. It was originally introduced by Lorentz (12) for calculating a local electric field in a system composed of electrically polarized particles but applies equally well for calculation of local magnetic fields created by a system of magnetically polarized particles—the so called magnetic susceptibility inclusions. In this approach, the susceptibility inclusions creating magnetic field at the position of the nucleus of interest are considered as point dipoles. Spatially they can be separated into nearby and distant by an imaginary Lorentzian Boundary. In most cases, a spherically shaped boundary, surrounding Lorentzian sphere, is widely adopted and the magnetic susceptibility shift of the Larmor frequency is evaluated as if the nucleus was moving inside an imaginary hollow sphere in a magnetized media with volume magnetic susceptibility χ—Eq. **2**.

Author contributions: X.H. and D.Y. designed research; X.H. and D.Y. performed research; X.H. and D.Y. analyzed data; and X.H. and D.Y. wrote the paper.

The authors declare no conflict of interest.

This article is a PNAS Direct Submission.

Freely available online through the PNAS open access option.

[1]To whom correspondence may be addressed. E-mail: hex@mir.wustl.edu or yablonskiyd@wustl.edu.

Here we suggest that due to the anisotropic and inhomogeneous nature of the brain's cellular structure (especially considering elongated cells, such as axons and dendrites), Eq. **2**, should be modified since the susceptibility inclusions cannot be modeled as point magnetic dipoles anymore. Indeed, at the subcellular level, protein-rich cytoskeleton fibers, lipid-rich endoplasmic reticulum and cell membranes, as well as iron-rich oligodendrocytes related to myelin, are primarily arranged in a highly anisotropic manner—mainly longitudinally along the axonal direction (13, 14). To see how this anisotropic arrangement affects susceptibility-induced MR signal frequency shift, consider first the following example. Imagine that we have a long axon oriented parallel to the magnetic field B_0. If one would use a standard Lorentzian sphere approximation, he/she would conclude that the magnetic susceptibility induced frequency shift of water molecules (residing outside of the susceptibility inclusions) would have been described by Eq. **2**, where the volume magnetic susceptibility χ contains the contribution from all of the susceptibility inclusions. Clearly this result is not correct because due to the longitudinal orientation of the above-mentioned structures in the axon with respect to the B_0, they would not create any magnetic field outside themselves, hence they would not create any shift of the NMR signal frequency.

To address this structural anisotropy of the cells, such as axons, dendrites, etc., we introduce a concept of a cylindrically shaped Lorentzian boundary (Lorentzian cylinder, or more generally—ellipsoid), rather than a spherically shaped Lorentzian boundary (Lorentzian sphere). This concept allows evaluation of the local susceptibility-driven frequency shifts of water in tissue due to the presence of the above mentioned longitudinal structures. Similar to the Lorentz sphere case, the effect of the field created by the inclusions within the Lorentzian cylinder on the nuclear Larmor frequency is negligible and the relative frequency shift due to such structures can be calculated as if the nuclei were moving inside a hollow cylinder in the homogeneous magnetized media with the magnetic susceptibility χ_a that includes only contributions from the longitudinal structures (see detail discussion in *Methods*). For a molecule, moving in such a hollow cylinder, frequency shift can be evaluated as:

$$\frac{\Delta f}{f_0} = 2 \cdot \pi \cdot \chi_a \cdot \sin^2 \vartheta, \qquad [3]$$

where ϑ is the angle between the axonal direction and the external field B_0. Of course, this frequency shift is additional to the frequency shift due to the isotropic part that can still be described by Eq. **2** with $\chi = \chi_{cell} - \chi_a$, where χ_{cell} is the total susceptibility of the cell, including longitudinal structures and cytosol. For orientation parallel to the magnetic field, this frequency shift disappears in agreement with the example described above.

If the imaging voxel contains many "long" cells with different orientations, the signal from such a structure should be calculated similarly to the case of a signal from a blood vessel network (15) as:

$$S(t) = S(0) \int d\vartheta \cdot P(\vartheta) \cdot \exp(-i \cdot 2 \cdot \pi \cdot \Delta f(\vartheta) \cdot t) \qquad [4]$$

where $P(\vartheta)$ is a distribution function of cells orientations. However, for short GRE times ($t \ll 1/\Delta f$), the accumulated phase of MRI signal is so small that a simple averaging of Eq. **3** will provide an adequate description of the signal frequency change. In particular, for random orientations of cylinders averaging of Eq. **3** leads to a result similar to Eq. **2**. This might provide a good approximation for GM where the directions of axons and dendrites form an almost uniform orientational distribution.

Hence, instead of Eq. **2**, the internal, cell-structure specific frequency shifts, Δf, due to the magnetic susceptibility effects can be approximated by the following equations:

$$\begin{aligned} \frac{\Delta f_{GM}}{f_0} &= \frac{4}{3} \cdot \lambda \cdot \pi \cdot \chi_{GM} \\ \frac{\Delta f_{WM}}{f_0} &= \frac{4}{3} \cdot \pi \cdot \chi_{WM} - 2 \cdot \pi \cdot \chi_a \cdot \left(\cos^2 \vartheta - \frac{1}{3} \right), \\ \frac{\Delta f_{CSF}}{f_0} &= \frac{4}{3} \cdot \pi \cdot \chi_{CSF} \end{aligned} \qquad [5]$$

The factor λ in the equation for GM reflects possible anisotropy of GM discussed above but in most cases could be set to unity. It is also important to note that the equation for WM is valid only for the imaging voxels where axonal fibers are all oriented in the same direction otherwise Eq. **4** should be used. The second term in Eq. **5** for WM reflects contribution of longitudinal structures to the susceptibility-induced MR signal frequency shift.

In addition to these internal, cell-structure specific frequency shifts described by Eq. **5**, the MR frequency shift also depends on the global tissue structure and interfaces per Eq. **1**. Let us consider an example of WM axonal fiber bundle that has a form of elliptical cylinder with main axis c and 2 orthogonal transverse axes a (long axes) and b (short axes). In this coordinate system the direction of magnetic field B_0 can be described by the angles α_c, α_a, and α_b with respect to the cylindrical and elliptical axes correspondingly. Then, it can be shown that the susceptibility-induced frequency shift of this WM bundle is

$$\begin{aligned} \frac{\Delta f}{f_0} = \frac{4}{3} \pi \cdot \chi_{WM} - 2\pi \cdot \chi_a \cdot \left(\cos^2 \alpha_c - \frac{1}{3} \right) \\ - 4\pi \cdot (\chi_{WM} - \chi_e) \cdot (N_a \cos^2 \alpha_a + N_b \cos^2 \alpha_b) \end{aligned} \qquad [6]$$

where χ_e is the magnetic susceptibility of the media outside the WM bundle, N_a and N_b are the demagnetizing factors of the ellipse [$N_a = b/(a + b)$, $N_b = a/(a + b)$ (16)]. The first term in this equation is a standard Lorentz sphere term that describes frequency shift that would exist if WM would have an isotropic structure, the second one is a correction to the Lorentz sphere term due to the presence of anisotropic structures, and the last one describes contribution of the demagnetizing field created due to the interface between WM axonal bundle and external media.

For a special case when direction of the bundle is along external magnetic field, Eq. **6** simplifies to

$$\frac{\Delta f}{f_0} = \frac{4}{3} \pi \cdot (\chi_{WM} - \chi_a). \qquad [7]$$

Hence, we come to a very important prediction of our theory—all of the longitudinal structures such as cytoskeleton filaments, myelin, etc. do not contribute to the MR signal frequency shift if they are oriented along the magnetic field. This is of course in agreement with our previous discussion.

Another special case is a circular axonal bundle in external isotropic media. For this case $N_a = N_b = 1/2$, and, recalling that $\cos^2\alpha_c + \cos^2\alpha_a + \cos^2\alpha_b = 1$, we obtain for a frequency difference between this bundle and the external media the following result:

$$\frac{\Delta f_{WM} - \Delta f_e}{f_0} = -2\pi \cdot (\chi_a - \chi_{WM} + \chi_e) \cdot \left(\cos^2 \alpha_c - \frac{1}{3} \right). \qquad [8]$$

It is important to note, that even in the case when magnetic susceptibility of WM is equal to the magnetic susceptibility of the

Table 1. Cellular content and related physical properties of the essential susceptibility inclusions in an "average normal" human frontal lobe cortical GM, WM, and CSF

	χ, ppm	GM, %	WM, %	CSF, %	Specific density
Water	−0.719 (29)	84	74	≈100	1.00
Proteins	−0.774 (30)	9.95	10.90	4.0E-3 (31)	1.335 (30)
Cholesterol	−0.735 (29)	1.28	4.24	0	1.07 (29)
Glycolipids	−0.670*	0.13	4.06	0	0.90†
Phospholipids	−0.670*	4.48	7.06	0	0.90†
Non-heme iron	0.11 (32)	4.0E-3 (33)	4.0E-3 (34)	3.0E-4 (35)	–

Fractions represent the percentage of total tissue wet weight. We use CGS units throughout. Magnetic susceptibility of all substances is volume susceptibility (in ppm) except for non-heme iron which is given in ppm per mg of iron per gram of tissue at 37° C. The data on GM/WM composition are from ref. 36.

*magnetic susceptibility of glycolipid and phospholipid is assumed to be the same as other fatty-acid- containing lipids (37).

†Specific density of glycolipids and phospholipids is assumed the same as the adipose tissue.

external media ($\chi_{WM} = \chi_e$), our theory in Eq. **8** still predicts the existence of a frequency shift. This would not be expected from a conventional theory based on the Lorentzian sphere approach, predicting 0 frequency shift in this case.

In addition to the cell-structure specific frequency shifts, deoxyhemoglobin in the blood vessel network also contributes to the GRE signal phase. This has been discussed previously (5, 17, 18), and here we only provide some useful relationships describing this effect. Assuming that the blood vessels are not arranged in any specific "orientationally preferred" fashion in both GM and WM, the Lorentz sphere concept can be applied and the frequency shift, Δf_d, of the extravascular MR signal due to the presence of deoxyhemoglobin in the blood can be evaluated as:

$$\frac{\Delta f_d}{f_0} = \frac{4}{3} \cdot \pi \cdot DBV \cdot Hct \cdot \Delta\chi_0 \cdot (1 - Y) \qquad [9]$$

where DBV is the Deoxyhemoglobin-containing Blood Volume fraction, Y is deoxyhemoglobin-containing blood oxygenation level, Hct is the blood hematocrit, and $\Delta\chi_0 = 0.27$ ppm (19) is the susceptibility difference between fully oxygenated and fully deoxygenated red blood cells. Comparing Eq. **9** with the contribution of the deoxyhemoglobin-containing blood to the GRE signal decay rate R_2' (17), the Lorentzian part of the frequency shift due to the presence of deoxygenated blood in the tissue can be expressed as $\Delta f_d = R_2'/2\pi$.

Tissue Magnetic Composition. The cellular composition of essential substances in human GM, WM, and CSF in frontal lobe and their related physical properties, that is, volume magnetic susceptibilities and densities, are listed in Table 1. While composition of proteins and lipids is relatively stable across different brain structures, the concentration of iron is highly variable and changes with age (see ref. 20 for an example).

It is worthwhile to first establish the contribution of each essential susceptibility inclusion to the magnetic susceptibilities of GM, WM, and CSF. Since both cytosol and interstitial fluid have very low concentration of soluble proteins lipids and other inclusions (21), as a first approximation we can estimate their magnetic susceptibility as for pure water. This however can be different in disease. Contributions to the tissue magnetic susceptibility from each component (relative to pure water) are listed in Table 2. Results are obtained based on the data from Table 1 and the following formula:

$$\chi_t = n_{ch} \cdot (\chi_{ch} - \chi_c) + n_l \cdot (\chi_l - \chi_c) + n_{pr} \cdot (\chi_{pr} - \chi_c) + w_{iron} \cdot \chi_{iron} + DBV \cdot Hct \cdot \chi_0 \cdot (1 - Y), \qquad [10]$$

where n_{pr}, n_{ch}, and n_l are the volume fractions (ml/ml) of proteins, cholesterol, and non-cholestrol lipids, respectively; w_{iron} and χ_{iron} are the concentration (mg/mL) and weight magnetic susceptibility (1/mg) of non-heme iron in tissue; the last term describes the volume magnetic susceptibility of deoxygenated blood. One can see that proteins are more diamagnetic than water. At the same time, lipids are less diamagnetic than water generating a "quasi-paramagnetic" contribution. It is interesting to note that the contributions of the diamagnetic proteins and paramagnetic non-heme iron in an "average normal" brain tissue almost cancel each other. Hence, the volume susceptibilities of both GM and WM are positive (relative to the water). The susceptibility of CSF is mainly determined by its non-heme iron content. Note that the WM susceptibility is very sensitive to iron concentration. In highly myelinated areas such as corpus callosum (38), or optic radiation (39), iron concentration is believed to be significantly lower. This would lead to a conclusion that the volume susceptibility of WM could become very close to or even smaller (more negative) than that of the water.

Experimental Results. Fig. 1 represents a typical example of an axial in vivo frequency shift image (b) and the corresponding T1 weighted image (a) acquired at the top of the brain in healthy volunteer. The B_0 field is applied perpendicular to the image plane. The frequency shift maps show similar in structure but higher in contrast-to-noise GM and WM contrast as compared to the corresponding T1 weighted image. On average, GM has a higher frequency than WM with a difference of 1.8 Hz (14.6×10^{-3} ppm). At the same time, the frequency of CSF located along the cortical GM is very similar to that of WM, although the detailed information cannot be extracted due to the low spatial resolution. These quantitative results are consistent with the previous experimental data for motor cortex area obtained at 7 T (5) listed in Table 3.

In the motor cortex area, the global geometrical orientation of the tissue boundaries and interfaces between GM, WM, and CSF can be approximated as parallel structures along the axis of the

Table 2. The volume magnetic susceptibility (relative to water) of "average normal" brain tissue in frontal lobe calculated according to Eq. 10, and Table 1

	GM, 10^{-3} ppm	WM, 10^{-3} ppm	CSF, 10^{-3} ppm
Proteins	−4.17	−4.56	−0.0016
Lipids	2.37	5.52	0
Non-heme iron	4.40	4.40	0.33
Deoxyhemoglobin	0.90	0.21	0
Total	3.50	5.57	0.33

The contributions from tissue compositions, i.e., protein, lipids, non-heme iron and deoxyhemoglobin, are listed separately. The contribution of deoxyhemoglobin was calculated based on the relationships $\Delta f_d = R_2'/2\pi$, $\Delta f_d/f_0 = 4/3\pi \cdot \chi_d$, and the R_2' values of 2.9 sec^{-1} (GM) and 0.68 sec^{-1} (WM) at 3T (8).

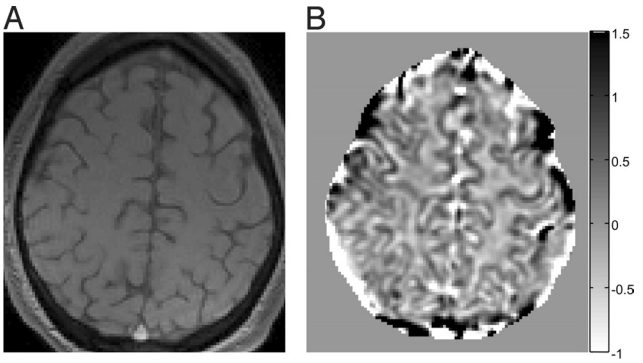

Fig. 1. Examples of T1 weighted axial magnitude images (*A*) and corresponding frequency shift maps in Hz (*B*) from a volunteer study. Images are from a slice close to the top of the brain. Image artifacts in the frequency map at the edges of the brain are due to partial volume effects.

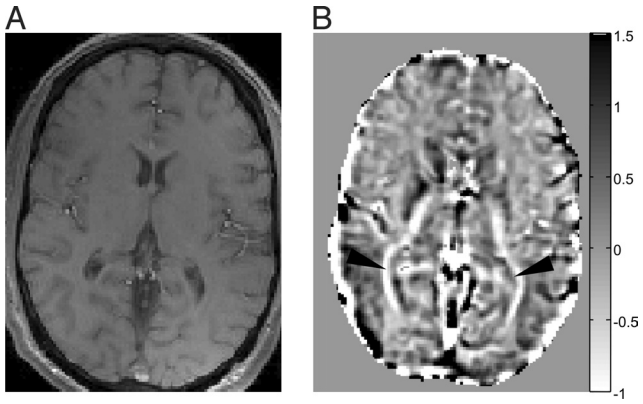

Fig. 2. Examples of T1 weighted axial magnitude images (*A*) and corresponding frequency shift maps in Hz (*B*) from a volunteer study. Images are from a slice close to the middle of the brain. Arrows point to the negative frequency bands in WM areas corresponding to the location of optic radiations fiber bundles (5).

main static field B_0. In this situation, inter-tissue boundaries do not contribute to the susceptibility-induced magnetic field and frequency shifts are described by Eq. **5**. In addition, since WM fibers in motor cortex area (also other areas at the top of the brain) are oriented mainly along the superior-inferior axis (parallel to the direction of B_0), the frequency shift in WM is described by Eq. **7**. Using Eqs. **5** and **7**, the frequency difference between GM and WM can be estimated as $+ 13.8 \times 10^{-3}$ ppm and between WM and CSF as -0.5×10^{-3} ppm, which agrees very well with the experimental data (see Table 3). On the other hand, if we use the Lorentzian sphere approximation as described in Eq. **2**, the estimated frequency differences between WM and GM and WM and CSF would be totally inconsistent with the experimental data (5). All of these results are listed in Table 3.

Consistent with the previous 7 T study (5), many anatomical structures that are not clearly delineated in T1-weighted images, such as globus pallidus, putamen, and the head of caudate nucleus, can be discriminated in the phase image as shown in Fig. 2. The observed higher frequency of these deep GM areas in Fig. 2*B*, can be explained by the large iron concentration. For example, iron concentrations have been measured around 200 μg/g tissue wet weight for globus pallidus, and around 100 μg/g tissue wet weight for putamen and caudate. From Table 1, we may conclude that these GM areas have volume susceptibility several times higher than the neighboring WM tissue. Therefore, these areas should have high frequency relative to the neighboring WM.

Similar to 7 T studies, the negative frequency in WM area at both hemispheres (arrows in Fig. 2*B*) correlates with the location of optic radiations fiber bundles (5). The negative frequency in optic radiations fiber bundles can be explained using generalized Lorentzian approach. Although due to the higher degree of myelination in optical radiation, the increase of the volume susceptibility due to the higher myelin content is overly negated by the lack of iron within the optical radiation. Therefore, we can conclude from Table 2 that the optical radiation might have susceptibility very close to or even less than that of the water. Since optical radiation fiber bundles can be approximately characterized as 2D planes oriented parallel to B_0 direction, the contribution of demagnetizing fields in Eq. **6** to their frequency shift is small leading to a lower frequency than neighboring tissues. The slight variation of phase contrast along optical radiation may correlate with the changes of fiber direction in the plane and/or bundle shape. Also, according to Eq. **6**, due to the decreased contribution of longitudinal structures to the WM susceptibility in these areas, the difference between generalized Lorentzian approach and traditional Lorentzian sphere approach may becom less significant. Accurate estimates however require knowledge of the tissue composition.

Table 3. The measured (5) and theoretically predicted frequency shifts, Δf ($\times 10^{-3}$ ppm), between different tissue types of motor cortex area

	Δf GM-WM	Δf GM-CSF	Δf WM-CSF
Measured (5)	15.7 ± 2.9	14.7 ± 1.3	−1.0 ± 3.3
Generalized Lorentzian approach	13.8	13.3	−0.5
Lorentzian sphere	−8.7	13.3	21.9

Note that only two of three frequency shifts are independent. In this brain area magnetic field B_0 is practically parallel to WM fibers and boundaries between WM, GM and CSF.

Discussion

In this manuscript, we investigated the origins of the tissue contrast seen in the phase images obtained with gradient recalled echo MRI. We demonstrated that this contrast depends on the tissue "magnetic architecture" at the subcellular and cellular levels. This architecture is mostly determined by the structural arrangements of proteins, lipids, non-heme tissue iron, and deoxyhemoglobin and their magnetic susceptibilities. Such magnetic environment affects/shifts frequencies of the MR signal generated by the water molecules moving/diffusing in the tissue. A theoretical framework allowing quantitative evaluation of the corresponding frequency shifts is developed based on the introduced concept of a generalized Lorentzian approximation. The difference between the proposed model and widely accepted Lorentzian Sphere model is most significant in the WM. The most striking demonstration of the validity of our model is explanation of the absence of the phase contrast between WM and CSF in the frontal lobe of the brain despite the substantial differences in WM and CSF magnetic susceptibilities.

Our theory provides quantitative relationships between GRE signal phase and the WM fiber orientations. This holds promise as additional information for fiber tracking applications. However, the tissue frequency shifts can be quantitatively modeled only when complete information about the geometric properties and the relative orientations at the subcellular and global tissue structure are taken into consideration. To fully understand the tissue phase contrast, the information from the phase images

could be analyzed together with the information obtained from diffusion tensor imaging.

Quantitative estimates provided in this manuscript are based on the average tissue composition for cortical GM and WM. In reality, WM composition can vary significantly among major fiber bundles and should be taken into consideration for interpretation of experimental data. Also in diseases such as stroke (22), Alzheimer's (23, 24), and multiple sclerosis (25), the total concentration or the composition of the lipids, proteins, and iron may be quite different from that of the normal brain. Therefore, the GRE MRI signal phase may provide additional information on these diseases.

The dependence of the phase contrast on the tissue microstructure could also aid in interpreting the phase contrast observed in MS lesions (10, 26) or other axonal injuries. Indeed, the sensitivity of tissue phase to the subcellular orientation of WM fibers indicates that the observed MRI signal phase may not directly relate to the volume magnetic susceptibility of the tissue. Moreover, our theory predicts that even if the total tissue composition does not change, the broken architecture of highly anisotropic tissue structures such as myelin or cytoskeleton neurofilaments can create phase contrast relative to a neighboring intact WM.

Conclusion

In this study, the possible origins of the phase contrast in GRE MRI of brain tissue were investigated. A theoretical framework allowing quantitative evaluation of tissue MRI signal frequency shifts due to the internal tissue-specific magnetic susceptibility effects is proposed. The concept of a generalized Lorentzian approximation is developed, which takes into account the specific geometric properties of the magnetic susceptibility inclusions in the brain tissue at the subcellular and global tissue levels. Such inclusions consist mainly of proteins, lipids, non-heme tissue iron, and deoxyhemoglobin. At the subcellular level, the WM inclusions are organized as structures arranged principally along the axonal direction. The predicted frequency contrast between GM, WM, and CSF in the motor cortex area agrees well with the previous experimental results and results obtained in this study. Both theory and experimental data demonstrated the sensitivity of the phase contrast to the relative orientation of the subcellular structure and the global geometry of the tissue with respect to the direction of the external magnetic field B_0. These effects of cellular composition and architecture hold promise for quantification of tissue microstructure based on the measurements of MRI signal phase. Also proposed mathematical relationships describing the dependence of the signal phase on the orientation of WM fibers, hold promise as additional information for fiber tracking applications.

Materials and Methods

Theory. The notion of a sphere of Lorentz is often used to estimate the local magnetic field at the nucleus of interest in the isotropic and homogeneous medium placed in the external homogeneous magnetic field B_0 [see for example (27)]. With this approach, the sources of this local magnetic field are considered as magnetic dipoles and are usually separated into nearby and distant by artificially selected spherical Lorentzian boundary around the nucleus. The size of this boundary is large enough compared to the distance between the sources so that the substance outside the boundary can be "seen" by the nucleus as a uniform macroscopic continuum. This boundary then will create a local magnetic field equal to $B_{Lorentz} = (4\pi/3)\cdot\chi\cdot B_0$ leading to the shift in the Larmor frequency described by Eq. **2**. For gases and liquids, the effect of magnetic fields created by the magnetic dipoles within the Lorentz boundary is negligible. Indeed, the rapid molecular motion leads to the nuclei uniformly sampling the spatial distribution of the fields created by nearby dipoles (recall that the average magnetic field created by a magnetic dipole is 0) leading to practically 0 contribution to the magnetic phase accumulated by moving nucleus (motional narrowing regime).

Here, we suggest that due to the anisotropic and inhomogeneous nature of the brain's cellular structure (especially considering elongated cells, such as axons and dendrites), Eq. **2** should be modified since the susceptibility inclusions cannot be modeled as point magnetic dipoles anymore. Clearly, if the inclusions are long cylinders or long ellipsoids arranged parallel to each other with the length much bigger than the distance between them, the spherical surface would not be a convenient way to separate contributions of nearby and distant sources. To take an advantage of the system symmetry, we use a cylindrical boundary (or elongated ellipsoidal boundary) which runs longitudinally along the inclusions around the nucleus of interest. Similar to the Lorentz sphere approach, sources outside Lorentz cylinder boundary can be considered as homogeneous media. Magnetic field created by this media in the hollow cylinder is $B_{Lorentz} = 2\cdot\pi\cdot\chi\cdot\sin^2\vartheta$, where ϑ is the angle between external filed B0 and the cylinder axis. Because the average magnetic field created by a linear source is 0, the rapid motion of the nucleus of interest around the linear sources inside the Lorentzian boundary will average out their contribution to a phase accumulated by this nucleus, leading to a negligible effect on MR frequency shift. Hence, the local magnetic field can be estimated *as if* the host nucleus was resided in the vacuum of the hypothetical cylindrical cavity.

In WM area, linear magnetic susceptibility inclusions consist of inclusions such as cytoskeleton fibers (neurofilaments) with the transverse size on the order of 0.1 μm and less (28), and WM myelin (including iron-rich oligodendrocytes) with the size on the order of several μm. For closely spaced neurofilaments, motion narrowing regime applies leading to negating of their contributions to the signal frequency shift as described above. Situation is different with the myelin which forms almost circular cylindrical surfaces around the axons. Since this surface has very low permeability for water molecules, it creates restrictions for water diffusion both in intracellular and extracellular spaces. The magnetic field created by myelin can be approximated as a magnetic field created by densely packed parallel cylinders. Using Lorentz cylinder approach, we can again separate contribution of these cylinders in the distant and nearby parts. The contribution of the distant part can still be described by Eq. **3**. Although an exact solution to the frequency shift due to the densely packed myelin cylinders within the cylindrical Lorentzian boundary is not known, based on the fact that the hexagonal close packed cylinders generate zero field at the center of the hexagon, we expect that the contribution from the near part of the cylinders to the MR signal frequency shift will be negligible, if not 0. The same conclusion can also be drawn under the static dephasing regime approximation where the phase of MR signal, originated from the nuclei filling the space between randomly distributed parallel cylinders within the cylindrical Lorentzian boundary, converges to 0 (17). Therefore, Eq. **3** is expected to be valid for the description of the susceptibility-induced frequency shifts originated from all linear sources within WM.

Experiment. All experiments were approved by Washington University's IRB and written informed consent was obtained from each recruited subject. A total of 3 studies were conducted on normal healthy volunteers. All images were acquired on a 3 T Trio whole body MRI scanner (Siemens Medical Systems). A standard receive-only 12-channel head coil was used. A 3D gradient echo sequence with 2 gradient echoes (TE of 3.6 ms and 21.6 ms) was used to acquire phase and magnitude images. FOV was $256 \times 192 \times 96$ mm^3 with image spatial resolution of $1.33 \times 1.33 \times 3$ mm^3. TR was 25 ms.

Raw data from the Siemens scanner were imported into Matlab (MathWorks Inc.) running on PC with a Pentium-4 CPU and 2 GB memory for image reconstruction and postprocessing. To avoid phase errors from multichannel coil sensitivity map, the phase images were reconstructed as follows. First, for each receiver channel, complex-value images corresponding to 2 echo times were reconstructed from the raw data. The phase of the complex division of the 2 images would be the phase evolution between the 2 echoes, eliminating any receiver dependent phase shifts. The final phase for each voxel was the normalized sum of phases from each channel, weighted by the relative channel sensitivity (calculated from a magnitude image at the first gradient echo). The frequency of the complex MRI signal was estimated based on the relationship: $\vartheta = \vartheta_0 + 2\cdot\pi\cdot f\cdot t$. All phase images were corrected for the macroscopic field inhomogeneities that were estimated by applying a Gaussian filter with full width at half maximum of 7 mm to the unwrapped phase images. The corrected phase images were then filtered by a Gaussian filter with FWHM of 1 voxel to increase SNR.

ACKNOWLEDGMENTS. We thank Drs. Joseph J.H. Ackerman, Marcus Raichle, Alex L. Sukstanskii, James D. Quirk, and Abraham Z. Snyder for useful discussions. This work was supported by National Institutes of Health Grants NS 055963 and P30NS048056 and a pilot grant from Mallinckrodt Institute of Radiology.

1. Haacke EM, Lai S, Yablonskiy DA, Lin W (1995) In vivo validation of the bold mechanism: A review of signal changes in gradient echo functional MRI in the presence of flow. *Int J Imaging Syst Technol* 6:153–163.
2. Yamada N, Imakita S, Sakuma T, Takamiya M (1996) Intracranial calcification on gradient-echo phase image: Depiction of diamagnetic susceptibility. *Radiology* 198:171–178.
3. Rauscher A, Sedlacik J, Barth M, Mentzel HJ, Reichenbach JR (2005) Magnetic susceptibility-weighted MR phase imaging of the human brain. *AJNR Am J Neuroradiol* 26:736–742.
4. Abduljalil AM, Schmalbrock P, Novak V, Chakeres DW (2003) Enhanced gray and white matter contrast of phase susceptibility-weighted images in ultra-high-field magnetic resonance imaging. *J Magn Reson Imaging* 18:284–290.
5. Duyn JH, et al. (2007) High-field MRI of brain cortical substructure based on signal phase. *Proc Natl Acad Sci USA* 104:11796–11801.
6. Marques JP, Maddage R, Mlynarik V, Gruetter R (2009) On the origin of the MR image phase contrast: An in vivo MR microscopy study of the rat brain at 14.1 T. *Neuroimage* 46:345–352.
7. Zhong K, Leupold J, von Elverfeldt D, Speck O (2008) The molecular basis for gray and white matter contrast in phase imaging. *Neuroimage* 40:1561–1566.
8. He X, Yablonskiy DA (2007) Quantitative BOLD: Mapping of human cerebral deoxygenated blood volume and oxygen extraction fraction: Default state. *Magn Reson Med* 57:115–126.
9. He X, Zhu M, Yablonskiy DA (2008) Validation of oxygen extraction fraction measurement by qBOLD technique. *Magn Reson Med* 60:882–888.
10. Hammond KE, et al. (2008) Quantitative in vivo magnetic resonance imaging of multiple sclerosis at 7 Tesla with sensitivity to iron. *Ann Neurol* 64:707–713.
11. ChuSC, Xu Y, Balschi JA, Springer CS, Jr (1990) Bulk magnetic susceptibility shifts in NMR studies of compartmentalized samples: Use of paramagnetic reagents. *Magn Reson Med* 13:239–262.
12. Lorentz HA (1909) in *The Theory of Electrons* (B.G. Teubners, Leipzig, New York), pp 132–139.
13. Maxwell WL, Domleo A, McColl G, Jafari SS, Graham DI (2003) Post-acute alterations in the axonal cytoskeleton after traumatic axonal injury. *J Neurotrauma* 20:151–168.
14. Tsukita S, Ishikawa H (1976) Three-dimensional distribution of smooth endoplasmic reticulum in myelinated axons. *J Electron Microsc (Tokyo)* 25:141–149.
15. Sukstanskii AL, Yablonskiy DA (2001) Theory of FID NMR signal dephasing induced by mesoscopic magnetic field inhomogeneities in biological systems. *J Magn Reson* 151:107–117.
16. Osborn JA (1945) Demagnetising factor for the general ellipsoid. *PhysRev* 67:351–356.
17. Yablonskiy DA, Haacke EM (1994) Theory of NMR signal behavior in magnetically inhomogeneous tissues: The static dephasing regime. *Magn Reson Med* 32:749–763.
18. Zhao F, Jin T, Wang P, Hu X, Kim SG (2007) Sources of phase changes in BOLD and CBV-weighted fMRI. *Magn Reson Med* 57:520–527.
19. Spees WM, Yablonskiy DA, Oswood MC, Ackerman JJ (2001) Water proton MR properties of human blood at 1.5 Tesla: Magnetic susceptibility, T(1), T(2), T*(2), and non-Lorentzian signal behavior. *Magn Reson Med* 45:533–542.
20. Haacke EM, et al. (2005) Imaging iron stores in the brain using magnetic resonance imaging. *Magn Reson Imaging* 23:1–25.
21. Srere PA (2000) Macromolecular interactions: Tracing the roots. *Trends Biochem Sci* 25:150–153.
22. Inuzuka T, et al. (1990) Changes in the concentrations of cerebral proteins following occlusion of the middle cerebral artery in rats. *Stroke* 21:917–922.
23. Soderberg M, Edlund C, Alafuzoff I, Kristensson K, Dallner G (1992) Lipid composition in different regions of the brain in Alzheimer's disease/senile dementia of Alzheimer's type. *J Neurochem* 59:1646–1653.
24. Englund E, Brun A, Alling C (1988) White matter changes in dementia of Alzheimer's type. Biochemical and neuropathological correlates. Brain 111:1425–1439.
25. Gerstl B, Eng LF, Tavaststjerna M, Smith JK, Kruse SL (1970) Lipids and proteins in multiple sclerosis white matter. *J Neurochem* 17:677–689.
26. Haacke EM, et al. (2009) Characterizing iron deposition in multiple sclerosis lesions using susceptibility weighted imaging. *J Magn Reson Imaging* 29:537–544.
27. Graf H, et al. (1976) Local magnetic field at a positive muon in ferromagnetic cobalt. *Phys Rev Lett* 37:1644–1647.
28. Hsieh ST, et al. (1994) Regional modulation of neurofilament organization by myelination in normal axons. *J Neurosci* 14:6392–6401.
29. Weast RC, Astle MC (1981–1982) in *CRC Handbook of Chemistry and Physics* (CRC Press, Cleveland, Ohio).
30. Savicki JP, Lang G, Ikeda-Saito M (1984) Magnetic susceptibility of oxy- and carbonmonoxyhemoglobins. *Proc Natl Acad Sci USA* 81:5417–5419.
31. Seyfert S, Kunzmann V, Schwertfeger N, Koch HC, Faulstich A (2002) Determinants of lumbar CSF protein concentration. *J Neurol* 249:1021–1026.
32. Schenck JF (1992) Health and physiological effects of human exposure to whole-body four-tesla magnetic fields during MRI. *Ann N Y Acad Sci* 649:285–301.
33. Griffiths PD, Crossman AR (1993) Distribution of iron in the basal ganglia and neocortex in postmortem tissue in Parkinson's disease and Alzheimer's disease. *Dementia* 4:61–65.
34. Chen JC, et al. (1989) T2 values in the human brain: Comparison with quantitative assays of iron and ferritin. *Radiology* 173:521–526.
35. Clardy SL, Earley CJ, Allen RP, Beard JL, Connor JR (2006) Ferritin subunits in CSF are decreased in restless legs syndrome. *J Lab Clin Med* 147:67–73.
36. Knaap MSvd, Valk J (2005) in *Magnetic Resonance of Myelination and Myelin Disorders* (Springer, New York), pp 7.
37. Szczepaniak LS, Dobbins RL, Stein DT, McGarry JD (2002) Bulk magnetic susceptibility effects on the assessment of intra- and extramyocellular lipids in vivo. *Magn Reson Med* 47:607–610.
38. Thomas LO, Boyko OB, Anthony DC, Burger PC (1993) MR detection of brain iron. *AJNR Am J Neuroradiol* 14:1043–1048.
39. Drayer B, et al. (1986) MRI of brain iron. *AJR Am J Roentgenol* 147:103–110.